

Erbium and Titanium Co-Doped Hematite Nanorods: Structural, Optical, and Catalytic Properties for Enhanced Water Splitting

Joan Talibawo, Pannan I. Kyesmen, Marie C. Cyulinyana, and Mmantsae Diale*

Herein, hydrothermally synthesized hematite nanorods (NRs) co-doped with erbium and titanium, using titanium tetrachloride and erbium(III) nitrate pentahydrate as the dopant sources, are presented. The effect of varied volumes of the erbium/titanium surface co-dopants on the morphology, structural, optical, and photoelectrochemical (PEC) properties of hematite NRs is investigated. The pristine hematite, 40 μL -Er, and 40 μL -Er/20 μL -Ti-doped NRs samples present a similar surface morphology of vertically aligned NRs. The NRs are randomly oriented with an increase in titanium dopant for the 40 μL -Er/30 μL -Ti-doped NRs and later coalesced for the 40 μL -Er/40 μL -Ti-doped NRs. The structural analysis based on X-ray diffraction and Raman analysis present a uniform, pure hematite phase for all the prepared NRs. The samples exhibit high photon absorbance with peaks in the 400–450 nm wavelength range of the visible spectrum. The 40 μL -Er/40 μL -Ti-doped NRs sample present the highest photocurrent density of 83.9 $\mu\text{A cm}^{-2}$ at 1.4 V vs reversible hydrogen electrode (RHE) and is attributed to the lowest flat band potential (−0.76 V vs RHE) that enhances charge mobility at the electrode–electrolyte interface. These results reveal the facile erbium/titanium doping of hematite NRs as a viable strategy for enhancing their PEC water-splitting performance.

1. Introduction

Decades after pioneering works on photoelectrochemical (PEC) water splitting using titanium dioxide (TiO_2) photoanodes by


Fujishima and Honda in 1972, the use of semiconductor photocatalysts for water splitting continues to be of significant interest in research for its feasible application in solar-driven hydrogen generation. Although the TiO_2 photoanodes exhibited great chemical stability in aqueous environments, a low quantum efficiency for water splitting was demonstrated mainly due to its wide bandgap (3.2 eV),^[1] which limited photon absorption to less than 5% within the visible spectrum range.^[1,2] This presented room for investigations on the PEC water-splitting potential of semiconductors with smaller bandgaps, which are equally stable in aqueous environments. Many stable semiconductors with smaller bandgaps compared to TiO_2 , stable in aqueous media, and with smaller bandgaps that enhance visible light absorption like tungsten oxide (WO_3),^[1] bismuth vanadate (BiVO_4),^[1,3] and hematite,^[4,5] have since been studied for PEC water splitting. Hematite has been extensively investigated due to its earth-abundance, small bandgap

of ≈ 1.8 –2.2 eV,^[6] favorable valence band edge position for water oxidation, and stability in a wide pH range.^[7,8] However, the reported solar-to-hydrogen conversion efficiency for hematite is still below the theoretically envisaged value of 17%.^[9] This is attributed to its poor electrical conductivity and the short hole diffusion length (2–20 nm) that greatly hinders the hole transfer at the semiconductor–electrolyte interface.^[10] Numerous strategies, like surface treatments, morphology modification, and incorporation of dopants, have been used to enhance the photocatalytic water splitting of hematite photoanodes.^[7]

The use of surface treatments is reported to improve the intrinsically slow oxygen evolution reaction kinetics at the semiconductor–electrolyte interface, subsequently improving the photocurrent performance of the electrode. For example, the use of a TiO_2 overlayer on hematite films enhanced the photocurrent density 4.5 times more compared to that of the bare hematite films.^[11] Another study by Xi et al.^[12] revealed a 44% increase in photocurrent density from 0.75 to 1.08 mA cm^{-2} at 0.23 V vs Ag/AgCl for hematite photoanodes after surface treatment with zinc acetate (ZnAc). Also, Tamirat et al.^[13] reported that the modification of planar photoanodes into various structures like nanoparticles, nanoflowers, and nanowires addresses the limitations of hematite's short hole diffusion length.

J. Talibawo, M. C. Cyulinyana
African Center of Excellence in Energy and Sustainable Development
University of Rwanda
PO, KN 67Street Nyarugenge, Kigali, Rwanda

J. Talibawo, P. I. Kyesmen, M. Diale
Department of Physics
University of Pretoria
Private Bag X20, Hatfield 0028, South Africa
E-mail: mmantsae.diale@up.ac.za

 The ORCID identification number(s) for the author(s) of this article can be found under <https://doi.org/10.1002/pssa.202200778>.

© 2023 The Authors. physica status solidi (a) applications and materials science published by Wiley-VCH GmbH. This is an open access article under the terms of the Creative Commons Attribution-NonCommercial-NoDerivs License, which permits use and distribution in any medium, provided the original work is properly cited, the use is non-commercial and no modifications or adaptations are made.

DOI: 10.1002/pssa.202200778

They further argue that nanostructured semiconductors offer a larger interfacial area for interaction with the electrolyte, which enhances charge generation and separation. Besides, 1D nanostructures, such as nanotubes, nanowires, and nanorods (NRs), are reported to offer wider surface area and higher aspect ratios for enhanced charge transport, which consequently cuts down on charge recombination when used in photocatalysis.^[14] For example, vertically oriented hematite NRs are highly commended for better photocatalytic performance than nanoparticles considering the narrow diameter that fits its short hole penetration distance.^[15] In addition, the use of dopants has been theoretically demonstrated to modify bandgaps of materials and lower their electron-effective mass.^[16] Comparably lower electron effective mass is reported to improve charge carrier speed which subsequently improves the photocurrent density outputs of photoelectrodes.^[16]

On account of enhancing photocurrent densities of hematite photoanodes through doping, a number of dopants have been studied, such as zinc (Zn),^[17] niobium (Nb),^[18] magnesium (Mg)^[19] and zirconium (Zr),^[20] titanium (Ti),^[15,21] and lanthanum (La).^[22] For instance, Ti as a dopant greatly improved the photocurrent density of hematite NRs by increasing the charge carrier density by two orders from 4.05×10^{17} to $1.49 \times 10^{19} \text{ cm}^{-3}$, which subsequently enhanced the photocurrent density.^[21] Zhang et al.^[23] also demonstrated an increase in conductivity for hematite photoanodes by ≈ 32 folds after doping with tantalum (Ta). Nonetheless, the use of rare earth metal dopants to improve the photocatalytic water-splitting potential of hematite photoanodes has not been extensively explored. In addition, the incorporation of rare-earth metal dopants in hematite films is reported to harness light absorption in the infrared radiation region and later emit the photons in the visible region.^[24,25] This subsequently contributes extra photons for absorption by the hematite photoanode.

To date, a number of preparation methods for pristine and doped hematite nanostructures, such as electrodeposition,^[26] spray pyrolysis,^[27,28] atomic layer deposition,^[25] spin coating,^[12] sol-gel,^[29] and hydrothermal method,^[15] have been used to investigate the various PEC water splitting enhancement strategies for hematite. For example, Annamalai et al.^[30] demonstrated the ex-situ Sn doping effect on the photocatalytic performance of hydrothermally synthesized hematite NRs. The hydrothermal method is largely characterized by its easy setup, modest energy usage, and scalable nature that allows control over the film structure and dimensions.^[31,32] Based on these advantages, the hydrothermal synthesis technique was preferred for the synthesis of hematite NRs in this study.

Herein, the influence of Er and Ti facile co-doping of hydrothermally synthesized hematite NRs was explored with a focus on the morphological, structural, optical, and catalytic properties. Although doped hematite NRs have widely been investigated, based on known reports in the literature, the effect of Er and Ti co-dopants on the properties of hydrothermally synthesized hematite NRs has not been reported. The results extracted from the X-ray diffraction (XRD) and Raman structural analysis of all photoanode samples presented a uniform hematite phase. The pristine, Er, and Er/Ti-doped hematite NRs also showed high absorption in the visible spectrum. The 40 μL -Er/40 μL -Ti-doped NRs presented the highest photocurrent density of $83.9 \mu\text{A cm}^{-2}$

at 1.4 V vs reversible hydrogen electrode (RHE), which was 31 times more compared to the pristine hematite NRs. This was highly associated with the lowest flat band potential and second highest charge density value exhibited by the 40 μL -Er/40 μL -Ti-doped NRs.

2. Results and Discussion

2.1. Morphology of Photoanodes

Figure 1 shows the morphology of the as-prepared samples obtained from the field emission scanning electron microscope (FE-SEM) measurements. The pristine NRs, 40 μL -Er-doped, and 40 μL -Er/20 μL -Ti-doped NRs samples presented relatively uniform topology of vertically aligned NRs arrays. Further increase in the Ti surface dopant volume with the 40 μL -Er/30 μL -Ti-doped NRs showed randomly oriented NRs, similar to a previous observation for ruthenium (Ru) doped hematite.^[33] The NRs in the 40 μL -Er/40 μL -Ti-doped NRs were observed to have coalesced. However, there were no observable traces of deposited dopant elements particles across the morphologies of the Er/Ti-doped NRs. This could be attributed to the small dopant concentrations and volumes applied. Overall, this result revealed that the surface doping of hematite NRs with Er and Ti dopants had no significant effect on their morphology with low dopant volumes, but as the volume increased, the morphology gradually changed, revealing a more coalesced surface morphology.

The cross-sectional images of the pristine and doped hematite NRs samples were further analyzed to establish their film thicknesses. **Figure 2** shows the cross-sectional view of the prepared samples. Film thicknesses of 569.1, 551.0, 498.1, 507.4, and 583.6 nm were determined for the pristine hematite, 40 μL -Er-doped, 40 μL -Er/20 μL -Ti, 40 μL -Er/30 μL -Ti, and 40 μL -Er/40 μL -Ti-doped NRs samples, respectively. The results indicated a decrease in film thickness as the dopant volume increased for the 40 μL -Er-doped and 40 μL -Er/20 μL -Ti-doped NRs when compared to the pristine hematite NRs. This is consistent with previous observations about the contraction of hematite NRs after facile doping with cobalt (Co) and tin (Sn).^[34] However, the thickness increased for the 40 μL -Er/30 μL -Ti and 40 μL -Er/40 μL -Ti-doped NRs samples. The increase in film thickness for the NRs could be due to the incorporation of Ti into the hematite phase and formation of a thin oxide layer with the increased Ti dopant concentration.^[35]

2.2. XRD and Raman Measurements

XRD measurements of doped hematite NRs were obtained to analyze the purity and crystallinity of the as-grown samples. **Figure 3** shows the XRD patterns of the pristine and Er/Ti-doped hematite NRs. According to JCPDS card no. 33-0664, peaks associated with hematite, including (012), (104), (110), (116), (214), (300), and (125) at 2θ angles of 24.3° , 33.15° , 35.61° , 54.09° , 62.45° , 63.99° , and 66.03° were observed across the XRD patterns.^[9] All samples revealed moderate peaks in (110) plane notable for enhanced charge separation and transport. The XRD result analysis indicated that the incorporation of the Er/Ti dopants did not alter the hematite structural phase

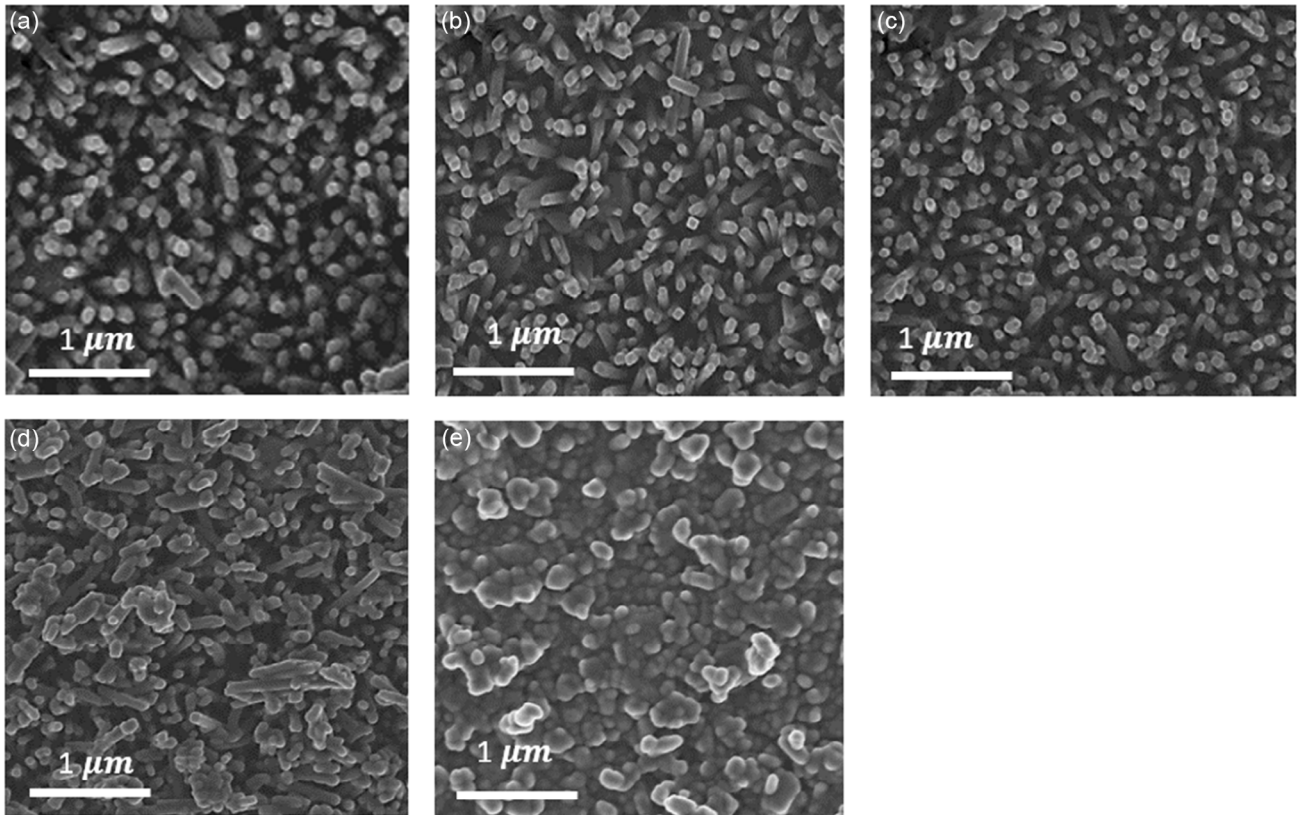


Figure 1. Topographic SEM images of a) pristine hematite NRs, b) 40 μL-Er-doped NRs, c) 40 μL-Er/20 μL-Ti-doped NRs, d) 40 μL-Er/30 μL-Ti-doped NRs, and e) 40 μL-Er/40 μL-Ti-doped NRs.

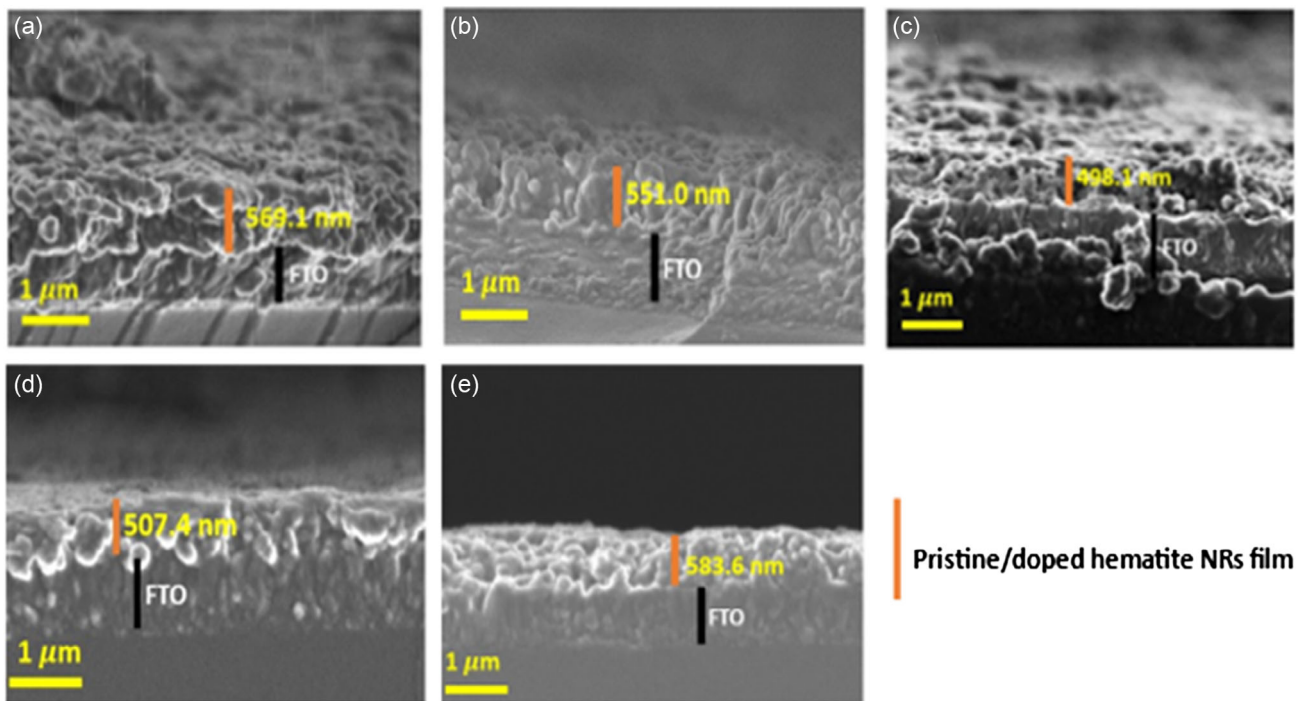


Figure 2. Cross-sectional images of a) pristine hematite NRs, b) 40 μL-Er, c) 40 μL-Er/20 μL-Ti, d) 40 μL-Er/30 μL-Ti, and e) 40 μL-Er/40 μL-Ti-doped-hematite NRs.

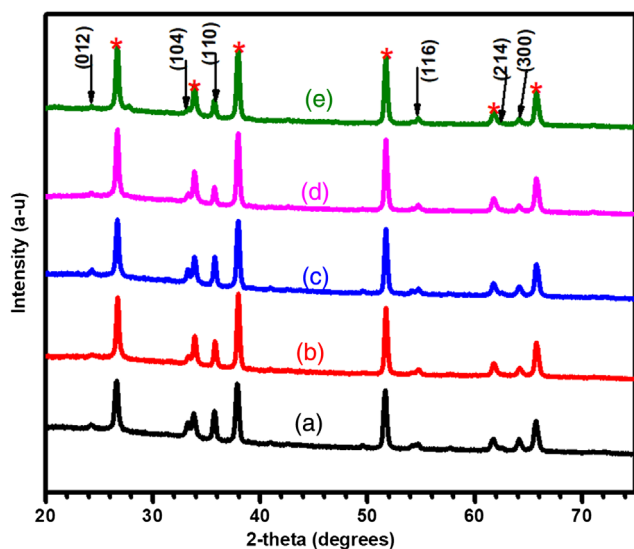


Figure 3. XRD diffraction pattern of a) pristine hematite NRs, b) 40 μ L-Er, c) 40 μ L-Er/20 μ L-Ti, d) 40 μ L-Er/30 μ L-Ti, and e) 40 μ L-Er/40 μ L-Ti-doped NRs.

since no other peaks associated with the Er/Ti dopants phases were observed. In addition, the distinct diffraction peaks are indicative of fine-crystallized samples.

In addition, the effect of the Er/Ti dopants on the crystal sizes of the samples was investigated using the Debye–Scherrer relation, $D = K\lambda/\beta\cos\Phi$, where D is the average crystal size, $K = 0.9$, which represents the Scherrer constant, $\lambda = 0.154$ nm and denotes the wavelength of the Cu $K\alpha$ -radiation, whereas β represents the full-width at half-maxima, and $\Phi = 2\theta/2$, is Bragg's angle.^[36] The crystal sizes obtained for the pristine hematite NRs, and Er/Ti-doped samples are shown in **Table 1**. The results reveal random variations in crystallite sizes as the dopant concentration increased over the pristine hematite NRs. First, the Er dopant increased the crystallite size of the 40 μ L-Er-doped NRs sample by 3.8 nm compared to 22.6 nm for the pristine hematite NRs. Contrary to previous observations,^[37] the increase in crystallite size could be associated with reduced solubility and substitution of Er ions into the hematite crystal lattice.^[29,38] This is similar to observations reported by Kumar et al.^[29] for doped hematite nanoparticles with concentrations of cerium (Ce) higher than 5%. Thereafter, the crystal sizes were reduced with an increase in the volume of the Ti dopant for the Er/Ti co-doped hematite NRs samples, consistent with the reported results.^[39] This observation also resonates with previous observations for

Table 1. Crystallite sizes based on (110) peak for pristine hematite and Er/Ti-doped hematite NRs.

NRs sample	Crystallite size [nm]
Pristine hematite NRs	22.6
40 μ L-Er-doped NRS	26.4
40 μ L-Er/20 μ L-Ti-doped NRs	25.9
40 μ L-Er/30 μ L-Ti-doped NRs	25.3
40 μ L-Er/40 μ L-Ti-doped NRs	24.7

facile copper (Cu)-doped hematite films and is ascribed to lower particle aggregation within the doped photoanodes.^[40] Furthermore, the incorporation of dopant ions into the host lattice is reported to increase the nucleation sites in hematite, which further allows more space for the growth of small crystallites.^[40] The pristine hematite and 40 μ L-Er-doped NRs samples exhibited the smallest and highest crystallite sizes of 22.6 and 26.4 nm, respectively. The smallest crystallite size for the pristine hematite photoanodes justifies the increased surface area for the nucleation and growth of crystallites alongside the vertically aligned NRs, which exhibited less coalescing, as observed in Figure 1.^[41,42] However, a further increase in Ti dopant volume for the 40 μ L-Er/40 μ L-Ti-doped NRs might have led to the coalescing of the NRs, and the formation of the oxide layer over the NRs as earlier described. This possibly contributed to the highest film thickness observed by the 40 μ L-Er/40 μ L-Ti-doped NRs (Figure 2). The peaks corresponding to the titanium oxide phases were not observed across the XRD spectra, possibly due to the low proportions of the dopant beyond the detectable margins of the instrument.^[43]

Raman spectroscopy measurements were conducted to confirm the structural phase presented by the XRD results. The Raman spectra of the NRs are shown in **Figure 4**. Seven active vibration modes expected for hematite were observed. These include two A_{1g} modes observed at 237 and 419 cm^{-1} and five E_g modes seen at 255, 301, 328, 510, and 622 cm^{-1} Raman shift positions, respectively. This further confirmed the hematite phase depicted by the XRD results. However, the E_g mode at 328 cm^{-1} was barely observed compared to other modes across the Raman spectra of the pristine, Er, and Ti-doped samples. Allietta et al.^[44] report similar observations of six clear Raman modes of silicon (Si)-doped hematite nanostructures. This observation might be attributed to a vibrational overlap of the close E_g modes at 301 and 328 cm^{-1} Raman shifts.^[45] However, it is important to note that the reflection of Raman vibrational modes at specific Raman shifts may vary due to

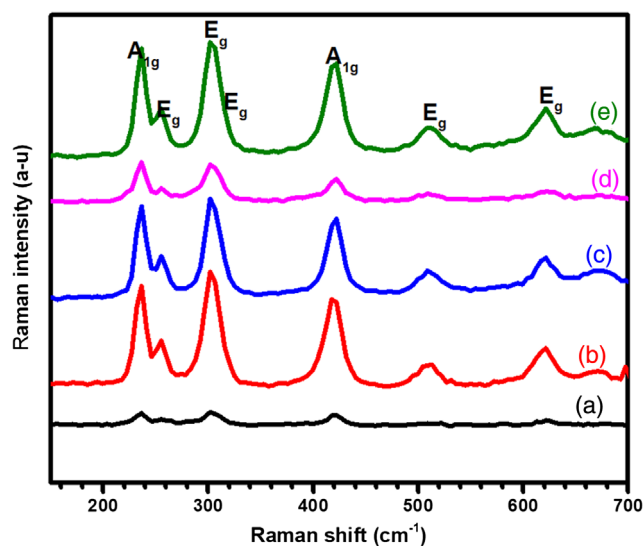


Figure 4. Raman shifts of a) pristine hematite NRs, b) 40 μ L-Er, c) 40 μ L-Er/20 μ L-Ti, d) 40 μ L-Er/30 μ L-Ti, and e) 40 μ L-Er/40 μ L-Ti-doped NRs.

the influence of preparation techniques, surface treatments, and incorporation of dopants.^[46]

2.3. Elemental Composition

The X-ray spectroscopy (EDS) spectra of the pristine and Er/Ti-doped hematite NRs were obtained to establish the species of elements in the films. The results revealed characteristic peaks of iron (Fe) and oxygen (O) at 6.4 and 0.52 keV, respectively, for all the samples. Furthermore, the peaks correlating with Er and Ti confirmed the presence of the dopant ions for the Er/Ti-doped samples, as shown in **Figure 5**. The tin (Sn) and silicon (Si) peaks

observed in the spectra were derived from the fluorine-doped tin oxide (FTO) substrates. These results confirm the successful incorporation of Er and Ti dopants into the hematite NRs.

2.4. Light Absorption Properties

UV–vis absorption data were used to examine the photon absorption of the pristine and Er/Ti-doped NRs photoanodes. **Figure 6** shows the absorption spectra pattern for the samples. All samples indicated strong light absorption in the visible spectrum with onsets at 600 nm wavelength. The pristine hematite NRs presented the highest absorption, ascribed to the favorable wide

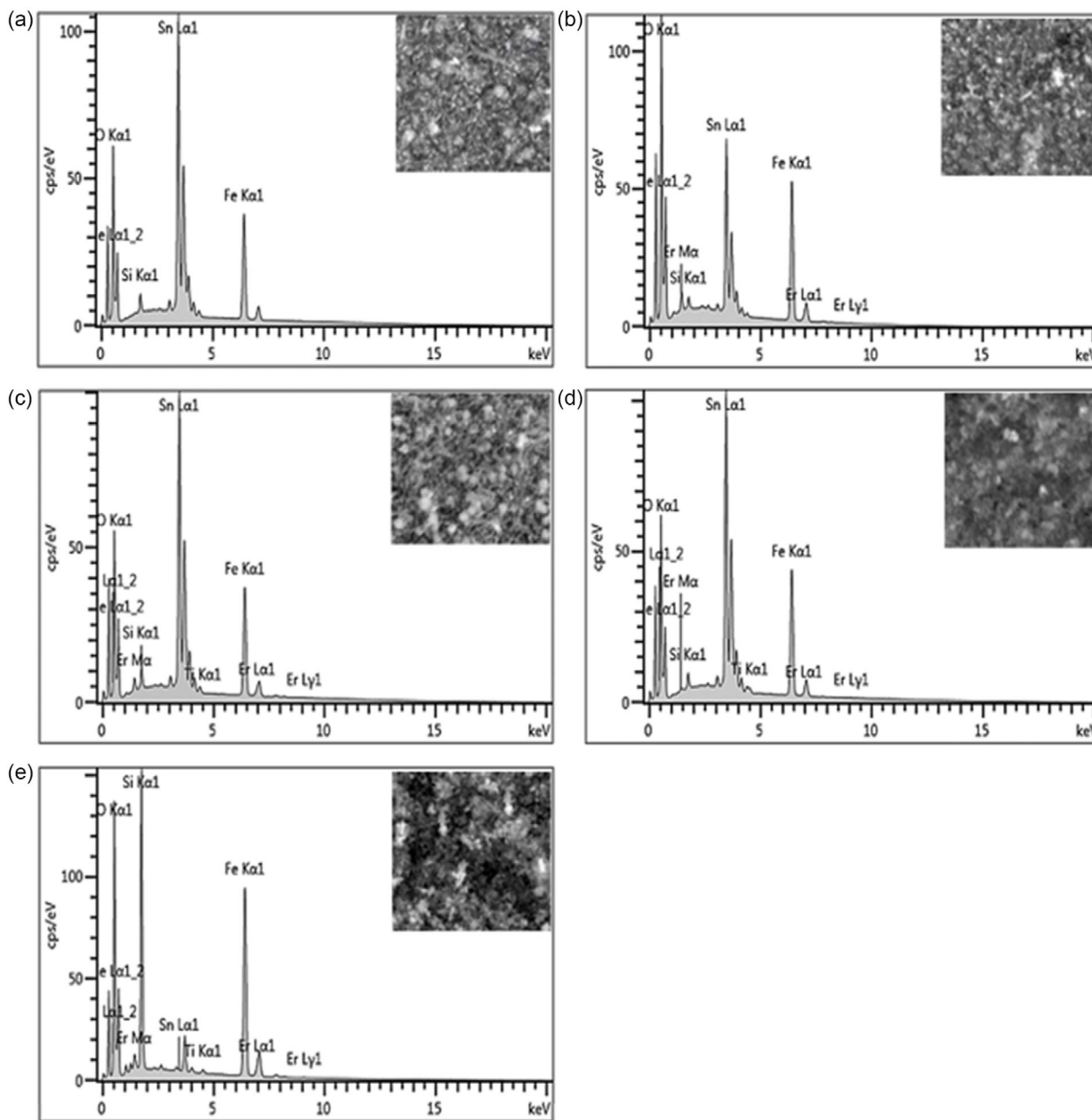


Figure 5. EDS spectra of a) pristine hematite NRs, b) 40µL-Er, c) 40µL-Er/20µL-Ti, d) 40µL-Er/30µL-Ti, and e) 40µL-Er/40µL-Ti-doped NRs.

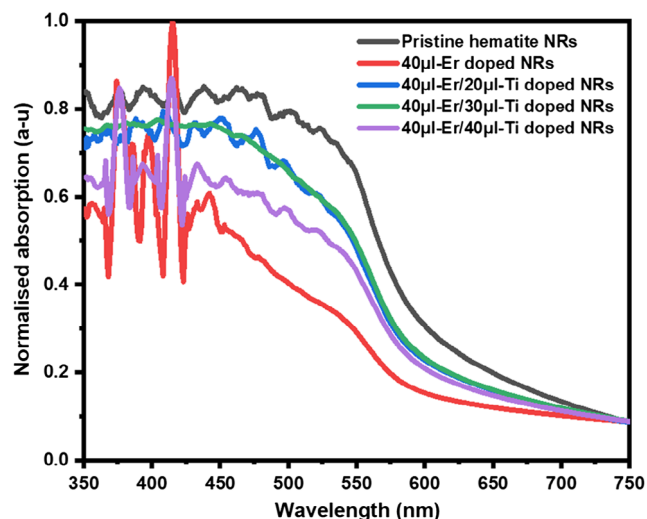


Figure 6. Normalized absorption and absorption spectra for pristine, Er, and Er/Ti-doped hematite NRs.

surface area presented by the vertically aligned NRs. In addition, this correlated with the second-highest film thickness exhibited by the pristine hematite NRs sample based on Beer–Lambert’s law, which linearly relates film absorbance with film thickness.^[5] The 40µl-Er-doped NRs sample also indicated strong absorption within the ≈370–420 nm range. This range is fitting and consistent with reported observations of enhanced absorption of hematite films within the visible spectrum (400–700 nm). The enhanced absorption for this sample could further be ascribed to the strong emitted photons associated to the Er dopant incorporated in the hematite lattice.^[24] Beyond this range, the Er dopant drastically lowered the absorption of pristine hematite NRs. The absorption of the photoanode samples thereafter increased with decrease in Ti dopant volumes against a constant Er dopant on the hematite NRs. The high absorption for the pristine hematite, 40µl-Er/20µl-Ti, and the 40µl-Er-doped NRs could be associated with the similar morphology of vertically aligned NRs, which provides the films with more surface area for light absorption than the coalesced NRs (Figure 1). The clustering and coalescing of the NRs arrays of the as-grown samples might have limited the effective surface area aspect for 40 µl-Er/30 µl-Ti, and 40 µl-Er/40 µl-Ti-doped NRs, thus lowering the photon absorption.^[5] In addition, the doped samples presented higher photon absorption with increasing crystallite size within the ≈350–450 nm range. Truffault et al.^[47] reported similar observations for hematite nanoparticles prepared for ultraviolet filtration. Overall, the differences in photon absorption can be attributed to the synergistic influence of crystallite size, sample morphology, thickness, and the incorporation of the Er/Ti dopant ions.

The Tauc relation $ah\nu = A(h\nu - E_g)^2$, where a represents the absorption coefficient, h the planks constant, ν stands for the frequency of light, A symbolizes an energy constant, and E_g denotes the bandgap was used to estimate the indirect optical bandgap values of the as-prepared pristine and doped hematite NRs samples. The bandgaps of the samples were determined from the $h\nu$ -axis intercepts values, obtained by extrapolating the linear section of the curves from the $(ah\nu)^2$ vs. $h\nu$ plots of the NRs samples, as

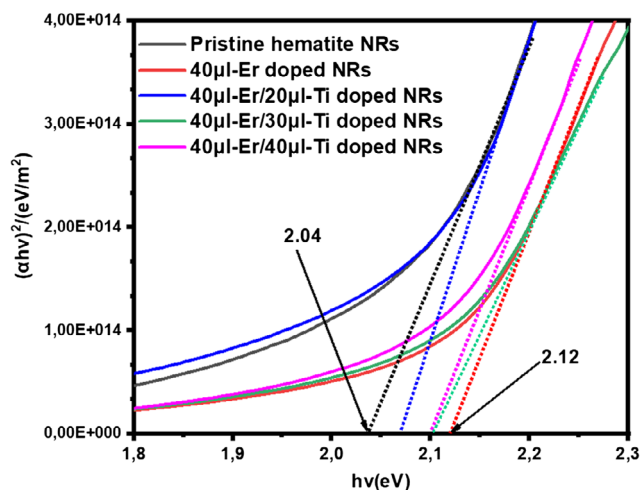


Figure 7. Tauc plots for pristine, erbium, and erbium/titanium doped hematite NRs.

shown in **Figure 7**. The estimated bandgap values for all the samples were within 2.04–2.12 eV range. This range is consistent with reported bandgap values for hematite NRs.^[5,19] The bandgaps of all the Er/Ti-doped NRs samples slightly increased by at least 1% compared to the 2.04 eV for the pristine hematite NRs, consistent with previous findings associated with sulfur (S) facile doped hematite.^[48] This shift highlights the improvement in photon absorption by the Er and Er/Ti-doped hematite NRs samples.^[49] This study shows that Er, as well as Er/Ti co-dopants, can improve the photon absorption of hematite in the visible light spectrum.

2.5. Photocurrent Density Measurements

Figure 8 shows the photocurrent density measurements for the pristine, Er, and Er/Ti-doped hematite NRs photoelectrode samples. The pristine hematite NRs yielded the least photocurrent of

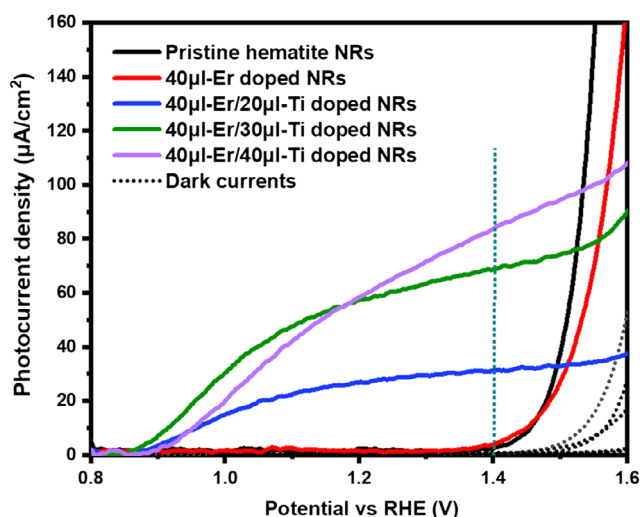


Figure 8. Current–voltage plots for pristine, Er, and Er/Ti-doped hematite NRs.

$2.72 \mu\text{A cm}^{-2}$ at 1.4 V vs RHE. However, a $1.58 \mu\text{A cm}^{-2}$ increase in photocurrent density was realized after doping the bare hematite NRs with Er at the same potential. The $40 \mu\text{L}$ -Er-doped NRs sample presented the second lowest photocurrent density despite its high Er dopant volume. This may be ascribed to increased resistivity widely demonstrated by ferrous films incorporated with rare earth metal ions like Er^{+3} .^[50] Thereafter, the photocurrent density increased across the samples with increase in Ti dopant volume up to $83.9 \mu\text{A cm}^{-2}$ at 1.4 V vs RHE for the $40 \mu\text{L}$ -Er/ $40 \mu\text{L}$ -Ti-doped NRs sample: ≈ 31 fold higher than the value obtained for the pristine hematite NRs. This observation is comparable with previous reports where Ti dopant was demonstrated to enhance conductivity of hematite photoanodes and separation of charges during PEC reactions.^[26,51] The enhanced photocurrent density highlights the role of the Ti dopant in tuning the electronic structure of hematite for enhanced conductivity.^[52,53] However, the moderate peak presentation observed for all the NRs samples in the (110) plane might have hindered the charge mobility resulting into high electron-hole pair recombination and subsequently the low photocurrent density values realized.^[54]

2.6. Mott-Schottky Analysis

Mott-Schottky plots of the pristine, Er, and Er/Ti-doped hematite NRs (Figure 9) were obtained from graphs of $1/C^2$ (F^{-2}) against potential (V vs RHE). The plots were analyzed to estimate the donor density (N_D) and flat band potential (V_{fb}) values of the NRs-based photoanodes using the expression in Equation (1)

$$\frac{1}{C^2} = \frac{2}{qA^2\epsilon\epsilon_0N_D} [(V - V_{fb}) - kT/q] \quad (1)$$

where C is the space charge capacitance, q is the electron charge ($1.602 \times 10^{-19} \text{C}$), ϵ is the dielectric constant for hematite (80), ϵ_0 is the permittivity of free space ($8.854 \times 10^{-12} \text{Fm}^{-1}$), A is the illuminated photoelectrode's surface area immersed in the

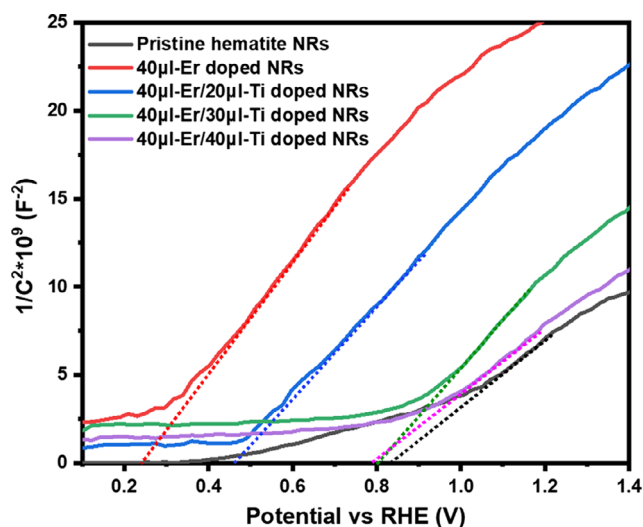


Figure 9. Mott-Schottky results for the pristine, Er, and Er/Ti hematite-doped NRs.

Table 2. V_{fb} and N_D values for pristine and Er/Ti-doped hematite NRs.

NRs sample	V_{fb} [V]	$N_D \times 10^{19} [\text{cm}^{-3}]$
Pristine hematite NRs	-0.31	3.91
40 μL -Er-doped NRS	-0.25	1.76
40 μL -Er/20 μL -Ti-doped NRs	-0.46	2.21
40 μL -Er/30 μL -Ti-doped NRs	-0.80	2.17
40 μL -Er/40 μL -Ti-doped NRs	-0.76	3.50

electrolyte, V denotes the applied potential at the photoanode, k represents Boltzmann's constant ($1.381 \times 10^{-23} \text{JK}^{-1}$), and T is the absolute temperature.^[55,56] The V_{fb} values were estimated using the x -axis intercepts of the linearly fitted sections of the plots, whereas the N_D values were obtained from the slopes (S) based on the relation $N_D = 2/SA^2q\epsilon\epsilon_0$. Table 2 shows the V_{fb} and N_D values for the different photoelectrodes.

The pristine hematite NRs revealed a V_{fb} of -0.31V . Thereafter, the facile doping of the hematite NRs with Er increased the V_{fb} by 0.06V . However, this observation is quite contrary to results reported on the enhancement of PEC properties of hematite photoanodes through incorporating rare earth elements in the semiconductor. This could be associated with the low Er dopant volume used.^[57,58] Furthermore, co-doping of the NRs with Er and Ti showed a cathodic shift of V_{fb} values with increase in the Ti dopant volume for the $40 \mu\text{L}$ -Er/ $20 \mu\text{L}$ -Ti and $40 \mu\text{L}$ -Er/ $30 \mu\text{L}$ -Ti-doped NRs samples. This observation is reflective of enhanced charge separation at the photoanodes/electrolyte interfaces,^[58] likely associated with a reduction in the number of recombination sites with increase in the Ti dopant.^[59] There was no significant difference in V_{fb} values obtained for the $40 \mu\text{L}$ -Er/ $30 \mu\text{L}$ -Ti and $40 \mu\text{L}$ -Er/ $40 \mu\text{L}$ -Ti-doped samples. This correlates with observations from previous studies where an increase in dopant concentrations for hematite films revealed no significant change in V_{fb} values.^[56,60]

The pristine hematite NRs exhibited the highest N_D value of $3.19 \times 10^{19} (\text{cm}^{-3})$. The vertically aligned NRs, which provide more surface area for light absorption and contact with the electrolyte, might have contributed to the highest N_D observed for the film.^[5] However, despite the highest N_D value, the pristine hematite revealed the second lowest photocurrent density among the samples. This was greatly associated with the more positive V_{fb} indicative of the slow charge carrier transfer kinetics at the semiconductor-electrolyte interface widely reported for hematite photoanodes, which eventually enhance charge recombination.^[61] The introduction of the Er dopant in the $40 \mu\text{L}$ -Er NRs electrode initially lowered the N_D by $2.15 \times 10^{19} (\text{cm}^{-3})$ when compared to $3.91 \times 10^{19} (\text{cm}^{-3})$ approximated for the pristine hematite NRs. However, the $40 \mu\text{L}$ -Er/ $20 \mu\text{L}$ -Ti-doped NRs revealed an improvement in N_D via facile Ti doping of the hematite NRs by at least 1.3 times compared to the $40 \mu\text{L}$ -Er NRs. The incorporation of Ti^{4+} dopant in the hematite lattice is shown to increase the concentration of electrons by transforming Fe^{3+} sites to Fe^{2+} to preserve the charge equilibrium.^[26,27] In so doing, extra charge carriers are generated, resulting in improved conductivity of the photoelectrode.^[26] The $40 \mu\text{L}$ -Er/ $40 \mu\text{L}$ -Ti-doped NRs presented the second highest N_D of $3.50 \times 10^{19} (\text{cm}^{-3})$, which coupled with the lowest V_{fb} likely contributed to the highest

photocurrent density obtained by the electrode sample. Furthermore, the formation of an oxide layer over the $40\mu\text{L-Er}/40\mu\text{L-Ti}$ -doped NRs sample as earlier discussed could have passivated the surface states of the photoelectrode sample consequently lowering the charge recombination.^[59,62] The Mott–Schottky analysis clearly reveal that Er/Ti doping improved the charge separation and transport dynamics of hematite NRs.

3. Conclusion

The structural, optical, and PEC properties of hydrothermally synthesized facile Er/Ti-doped hematite NRs were investigated.

The incorporation of Er/Ti dopants in the hematite lattice had no significant impact on the morphology for $40\mu\text{L-Er}$ and $40\mu\text{L-Er}/20\mu\text{L-Ti}$ -doped NRs since they presented vertically aligned NRs similar to those of the pristine hematite films. However, a further increase in dopant concentration for $40\mu\text{L-Er}/30\mu\text{L-Ti}$ and $40\mu\text{L-Er}/40\mu\text{L-Ti}$ -doped NRs showed coalesced NRs. The cross-section analysis of the samples revealed a 3.2% and 12.5% reduction in film thickness for the $40\mu\text{L-Er}$ and $40\mu\text{L-Er}/20\mu\text{L-Ti}$ -doped NRs compared to 569.1 nm for the pristine hematite NRs. Thereafter, the film thickness increased by $\approx 1.9\%$ for the $40\mu\text{L-Er}/30\mu\text{L-Ti}$ and $\approx 16.9\%$ for $40\mu\text{L-Er}/40\mu\text{L-Ti}$ -doped NRs compared to 498.1 nm of the $40\mu\text{L-Er}/20\mu\text{L-Ti}$ -doped NRs. The XRD and Raman results confirm a pure phase of hematite for the pristine and

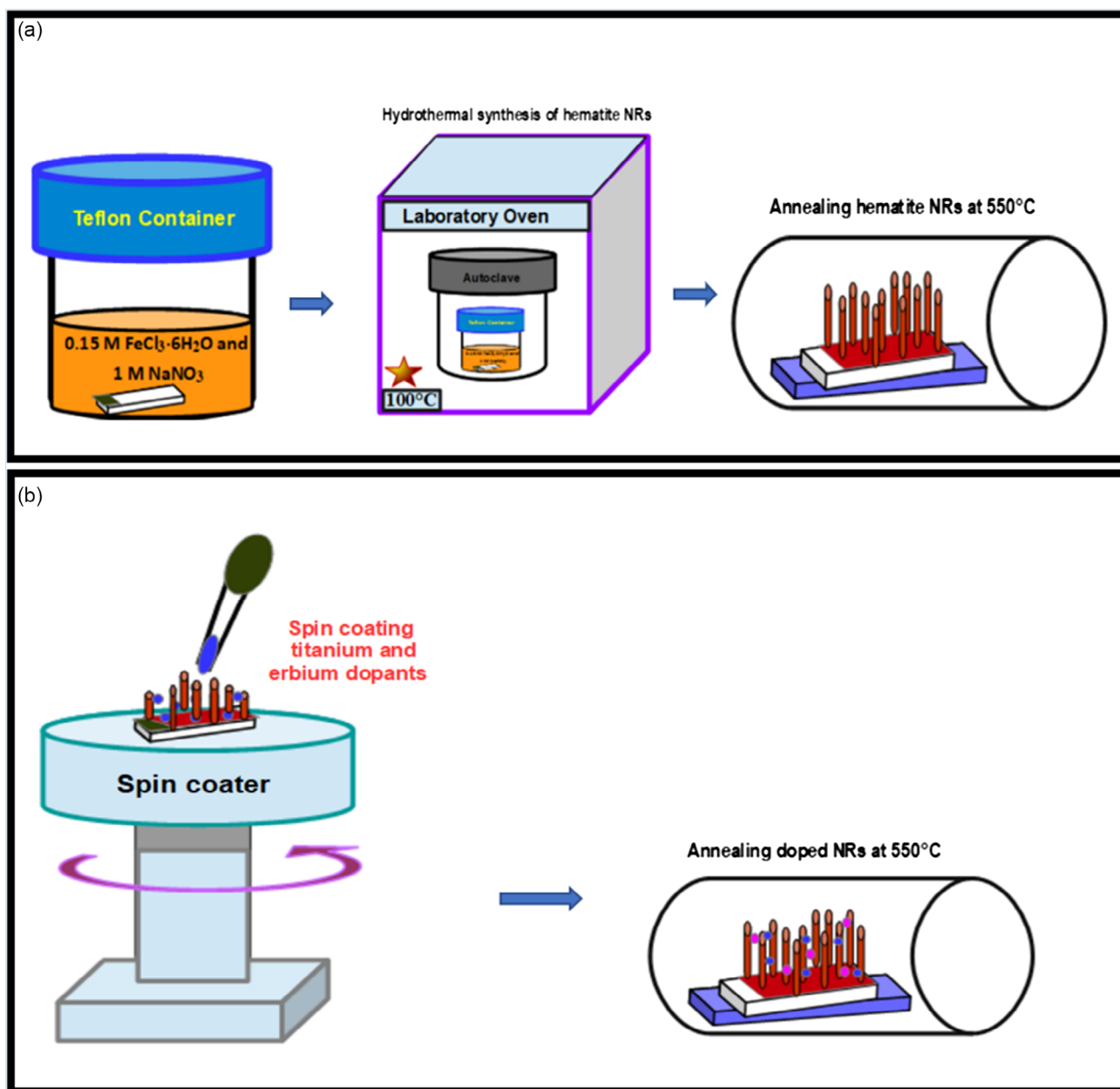


Figure 10. Schematic diagram of hydrothermal synthesis and annealing process of a) pristine hematite NRs, and b) Er/Ti co-doped hematite NRs.

Er/Ti-doped hematite NRs. All samples exhibited high absorption in the visible spectrum. The bandgap values obtained for the photoanode NRs samples were in the 2.04–2.12 eV range and closely corresponded with reported values for hematite films. According to the PEC results, the 40 μ L-Er/40 μ L-Ti-doped NRs produced the highest photocurrent density of 83.9 μ A cm^{-2} at 1.4 V vs RHE due to its high photon absorption, second highest donor density ($3.50 \times 10^{19} \text{cm}^{-3}$), and the second lowest flat band potential (−0.76 V). This study demonstrates the viable potential of facile Er/Ti-doped hematite NRs for photocatalytic water splitting.

4. Experimental Section

Materials: The hematite NRs were synthesized using ferric chloride ($\text{FeCl}_3 \cdot 6\text{H}_2\text{O}$, 97%), sodium nitrate (NaNO_3 , 98%), and hydrochloric acid (HCl, 32%). Titanium tetrachloride (TiCl_4 , 99%) and erbium(III) nitrate pentahydrate ($\text{Er}(\text{NO}_3)_3 \cdot 5\text{H}_2\text{O}$, 99%) were used for preparing the dopant solutions for the NRs. All chemicals were used as purchased from Sigma without further purification. Millipore deionized (DI) water was used as the solvent in the preparation of the precursor solutions.

Synthesis of Hematite NRs: FTO substrates were ultrasonically cleaned using sodium stearate ($\text{C}_{18}\text{H}_{35}\text{NaO}_2$) soap solution, ethanol, acetone and thoroughly rinsed with distilled water. The substrates were thereafter dried with nitrogen gas. Hematite NRs were then hydrothermally synthesized on the FTO substrates. Before film deposition, the nonconducting sides of the substrates and a small section of the conducting side were sealed with Kapton tape. The FTO substrates were then placed at the bottom of a Teflon container with the conducting side facing upwards. The container was filled with 45 mL of an aqueous solution containing 0.15 M $\text{FeCl}_3 \cdot 6\text{H}_2\text{O}$, 1 M NaNO_3 , and 0.125 mL of HCl. The container was covered, firmly sealed in a stainless-steel reactor, and heated in a laboratory oven at 100 °C for 10 h. Following this reaction, the oven was switched off and allowed to cool down to room temperature. Yellowish films of iron(III) oxyhydroxide (FeOOH) were observed on the substrates. The deposited films were then washed severally with DI water to get rid of extra reactants. The Kapton tape at the non-conducting side was removed, and the samples were dried using flowing nitrogen. Thereafter, the FeOOH films were annealed at 550 °C for 2 h to get pristine hematite NRs.

Doping of Hematite NRs: To prepare the titanium (Ti) dopant, 0.03 mL of titanium tetrachloride (TiCl_4) was added dropwise to 3 mL of (DI) water, whereas the erbium (Er) dopant was an aqueous solution of 0.1 M Er ($\text{NO}_3)_3 \cdot 5\text{H}_2\text{O}$. The pristine hematite NRs were facile doped with a fixed volume 40 μ L of Er dopant solution via the spin coating method at 3000 rpm to get the 40 μ L-Er-doped hematite NRs. Thereafter, 20, 30, and 40 μ L of the Ti dopant were spin-coated over the Er-doped samples to obtain the final 40 μ L-Er/20 μ L-Ti, 40 μ L-Er/30 μ L-Ti, and 40 μ L-Er/40 μ L-Ti-doped hematite NRs samples, respectively. All the doped samples were annealed further at 550 °C for 0.5 h to obtain crystallized Er and Er/Ti-doped NRs. **Figure 10** illustrates the sample preparation process. The pristine hematite NRs sample was also further treated to the same annealing conditions (550 °C for 0.5 h) to get the final sample used in the investigation.

Characterization: The surface morphologies of the as-prepared samples were examined using the Zeiss Ultra PLUS FE-SEM. An energy-dispersive EDS was coupled to the Zeiss crossbeam and used to examine the elemental composition of the NRs. The crystalline structural patterns of the NRs were obtained using $\text{CuK}\alpha$ radiation from a Bruker D2 Phaser X-ray diffractometer. The Raman vibrational spectra of the samples were examined using a $\lambda = 532$ nm green laser for excitation from a WITec alpha 300 RAS+ confocal micro-Raman microscope. The optical absorption measurements were performed using an Agilent Cary-60 UV–vis equipment, where a blank FTO substrate was used as a reference for background subtraction.

PEC measurements for the pristine and doped hematite NRs were carried out using a VersaSTAT 3F potentiostat from Princeton Applied Research, which was linked to a three-electrode PEC cell assembled in a Teflon container with a 0.49 cm^2 window provided for illumination. Illumination of 100 mW cm^{-2} was obtained from a Newport *Oriel* | LCS—1007M solar simulator calibrated using a Newport 91150 V reference cell. A 4 cm^2 platinum (Pt) mesh counter electrode, a silver/silver chloride (Ag/AgCl) in 3 M KCl reference electrode, and the pristine hematite, Er and Er/Ti-doped NRs synthesized on FTO substrates as working electrodes were dipped in a 1 M NaOH aqueous solution as the electrolyte ($\text{Ph} = 13.6$). Linear sweep voltammetry measurements were obtained with and without the illumination of the pristine hematite, Er, and Er/Ti-doped NRs with an applied potential sweep from −0.9 to 0.8 V vs Ag/AgCl, at a scan rate of 0.05 V s^{-1} to obtain their photocurrent density values. The Mott–Schottky measurements were recorded in the dark using a DC potential range of 1.2–0.5 V vs Ag/AgCl. All potential values obtained with Ag/AgCl reference electrode were converted to RHE scale using Equation (2).^[9]

$$E_{\text{RHE}} = E_{\text{Ag/AgCl}} + (0.059\text{Ph}) + E^0_{\text{Ag/AgCl}} \quad (2)$$

In this equation, E_{RHE} is the potential in the RHE scale, $E_{\text{Ag/AgCl}}$ denotes the potential obtained with the Ag/AgCl electrode during the experiment, and $E^0_{\text{Ag/AgCl}} = 0.1976 \text{V}$ at 25 °C.

Acknowledgements

This work was made possible by the financial support from the African Centre of Excellence in Energy and Sustainable Development at the University of Rwanda, Department of Physics-University of Pretoria, The National Research Foundation, competitive program for rated researcher project number 118520; NRF-DST SARCHI Grant number 115463, The Organization for Women in Science for the Developing World (OWSD), and Swedish International Development Cooperation Agency (SIDA).

Conflict of Interest

The authors declare no conflict of interest.

Data Availability Statement

The data that support the findings of this study are available from the corresponding author upon reasonable request.

Keywords

erbium/titanium co-doped, hematite nanorods, photocatalyst, photoelectrochemical water oxidation

Received: November 15, 2022

Revised: January 31, 2023

Published online: March 30, 2023

- [1] Y. Pihosh, I. Turkevych, K. Mawatari, T. Asai, T. Hisatomi, J. Uemura, M. Tosa, K. Shimamura, J. Kubota, K. Domen, *Small* **2014**, *10*, 3692.
- [2] A. Fujishima, K. Honda, *Nature* **1972**, *238*, 37.
- [3] M. Tayebi, B.-K. Lee, *Renew. Sustain. Energy Rev.* **2019**, *111*, 332.
- [4] A. Rokade, Y. Jadhav, S. Jathar, S. Rahane, S. Barma, G. Rahane, S. Thawarkar, P. Vairale, A. Punde, S. Shah, *Eng. Sci.* **2021**, *17*, 242.
- [5] J. Talibawo, J. S. Nyarige, P. I. Kyesmen, M. C. Cyulinyana, M. Diale, *Mater. Res. Express* **2022**, *9*, 026401.

- [6] O. Zandi, T. W. Hamann, *Phys. Chem. Chem. Phys.* **2015**, *17*, 22485.
- [7] S. Ho-Kimura, B. A. Williamson, S. Sathasivam, S. J. Moniz, G. He, W. Luo, D. O. Scanlon, J. Tang, I. P. Parkin, *ACS Omega* **2019**, *4*, 1449.
- [8] S. Li, J. Cai, Y. Mei, Y. Ren, G. Qin, *Int. J. Photoenergy*, **2014**, 2014, 1.
- [9] P. I. Kyesmen, N. Nombona, M. Diale, *J. Alloys Compd.* **2021**, *863*, 158724.
- [10] S. Kment, F. Riboni, S. Pausova, L. Wang, L. Wang, H. Han, Z. Hubicka, J. Krysa, P. Schmuki, R. Zboril, *Chem. Soc. Rev.* **2017**, *46*, 3716.
- [11] M. G. Ahmed, I. E. Kretschmer, T. A. Kandiel, A. Y. Ahmed, F. A. Rashwan, D. W. Bahnemann, *ACS Appl. Mater. Interfaces* **2015**, *7*, 24053.
- [12] L. Xi, P. S. Bassi, S. Y. Chiam, W. F. Mak, P. D. Tran, J. Barber, J. S. C. Loo, L. H. Wong, *Nanoscale* **2012**, *4*, 4430.
- [13] A. G. Tamirat, J. Rick, A. A. Dubale, W.-N. Su, B.-J. Hwang, *Nanoscale Horizons* **2016**, *1*, 243.
- [14] Y. Lin, G. Yuan, R. Liu, S. Zhou, S. W. Sheehan, D. Wang, *Chem. Phys. Lett.* **2011**, *507*, 209.
- [15] Z. Fu, T. Jiang, Z. Liu, D. Wang, L. Wang, T. Xie, *Electrochim. Acta* **2014**, *129*, 358.
- [16] X. Meng, G. Qin, W. A. Goddard III, S. Li, H. Pan, X. Wen, Y. Qin, L. Zuo, *J. Phys. Chem. C* **2013**, *117*, 3779.
- [17] S. Kumari, C. Tripathi, A. P. Singh, D. Chauhan, R. Shrivastav, S. Dass, V. R. Satsangi, *Curr. Sci.* **2006**, 1062.
- [18] Y. Fu, C. L. Dong, W. Y. Lee, J. Chen, P. Guo, L. Zhao, S. Shen, *ChemNanoMat* **2016**, *2*, 704.
- [19] S. Y. Chiam, M. H. Kumar, P. S. Bassi, H. L. Seng, J. Barber, L. H. Wong, *ACS Appl. Mater. Interfaces* **2014**, *6*, 5852.
- [20] S. Shen, P. Guo, D. A. Wheeler, J. Jiang, S. A. Lindley, C. X. Kronawitter, J. Z. Zhang, L. Guo, S. S. Mao, *Nanoscale* **2013**, *5*, 9867.
- [21] D. Wang, H. Chen, G. Chang, X. Lin, Y. Zhang, A. Aldabahi, C. Peng, J. Wang, C. Fan, *ACS Appl. Mater. Interfaces* **2015**, *7*, 14072.
- [22] N. Li, S. Jayaraman, S. Y. Tee, P. S. Kumar, C. J. Lee, S. L. Liew, D. Chi, T. A. Hor, S. Ramakrishna, H.-K. Luo, *J. Mater. Chem. A* **2014**, *2*, 19290.
- [23] H. Zhang, D. Li, W. J. Byun, X. Wang, T. J. Shin, H. Y. Jeong, H. Han, C. Li, J. S. Lee, *Nat. Commun.* **2020**, 11.
- [24] T. J. Mullen, M. Zhang, W. Feng, R. J. El-Khoury, L.-D. Sun, C.-H. Yan, T. E. Patten, G.-y. Liu, *ACS Nano* **2011**, *5*, 6539.
- [25] M. Zhang, Y. Lin, T. J. Mullen, W.-F. Lin, L.-D. Sun, C.-H. Yan, T. E. Patten, D. Wang, G.-Y. Liu, *J. Phys. Chem. Lett.* **2012**, *3*, 3188.
- [26] N. Mirbagheri, D. Wang, C. Peng, J. Wang, Q. Huang, C. Fan, E. E. Ferapontova, *ACS Catal.* **2014**, *4*, 2006.
- [27] S. Kumari, A. P. Singh, D. Deva, R. Shrivastav, S. Dass, V. R. Satsangi, *Int. J. Hydrogen Energy* **2010**, *35*, 3985.
- [28] J. S. Nyarige, T. P. Krüger, M. Diale, *Phys. B: Condens. Matter* **2020**, *581*, 411924.
- [29] V. Kumar, D. S. Ahlawat, S. A. Islam, A. Singh, *Mater. Sci. Eng.: B* **2021**, *272*, 115327.
- [30] A. Annamalai, P. S. Shinde, T. H. Jeon, H. H. Lee, H. G. Kim, W. Choi, J. S. Jang, *Sol. Energy Mater. Sol. Cells* **2016**, *144*, 247.
- [31] M. Khalil, J. Yu, N. Liu, R. L. Lee, *J. Nanoparticle Res.* **2014**, 16.
- [32] S. Yang, P. Y. Zavalij, M. S. Whittingham, *Electrochem. Commun.* **2001**, *3*, 505.
- [33] C. L. Ndlangamandla, K. Bharuth-Ram, O. M. Ndwandwe, B. D. Ngom, M. Maaza, *J. Nanopart.*, **2015**, 2015.
- [34] J. Wang, C. Du, Q. Peng, J. Yang, Y. Wen, B. Shan, R. Chen, *Int. J. Hydrogen Energy* **2017**, *42*, 29140.
- [35] S. Shen, J. Zhou, C.-L. Dong, Y. Hu, E. N. Tseng, P. Guo, L. Guo, S. S. Mao, *Sci. Rep.* **2014**, 4.
- [36] I. Hamdani, A. N. Bhaskarwar, *Sol. Energy Mater. Sol. Cells* **2022**, *240*, 111719.
- [37] N. Popov, M. Ristić, V. Kuncser, K. Zadro, N. Velinov, P. Badica, A. Alexandru-Dinu, N. Iacob, L. K. Krehula, S. Musić, *J. Phys. Chem. Solids* **2022**, *169*, 110857.
- [38] K. Rekha, M. Nirmala, M. G. Nair, A. Anukaliani, *Phys. B: Condens. Matter* **2010**, *405*, 3180.
- [39] T. S. Atabaev, M. Ajmal, N. H. Hong, H.-K. Kim, Y.-H. Hwang, *Appl. Phys. A* **2015**, *118*, 1539.
- [40] S. Haider, S. S. Shar, I. Shakir, P. O. Agboola, *Ceram. Int.* **2022**, *48*, 7605.
- [41] A. Ali, X. Zhao, A. Ali, L. Duan, H. Niu, C. Peng, Y. Wang, S. Hou, *Superlattices Microstruct.* **2015**, *83*, 422.
- [42] J. Sun, L. Sun, X. Yang, S. Bai, R. Luo, D. Li, A. Chen, *Electrochim. Acta* **2020**, *331*, 135282.
- [43] M. Ristić, E. Kuzmann, Z. Homonnay, S. Musić, *J. Alloys Compd.* **2018**, *767*, 504.
- [44] M. Allieta, M. Marelli, F. Malara, C. L. Bianchi, S. Santangelo, C. Triolo, S. Patane, A. M. Ferretti, Š. Kment, A. Ponti, *Catal. Today* **2019**, *328*, 43.
- [45] J. S. Nyarige, T. P. Krüger, M. Diale, *Surf. Interfaces* **2020**, *18*, 100394.
- [46] A. Zoppi, C. Lofrumento, E. Castellucci, P. Sciau, *J. Raman Spectrosc.* **2008**, *39*, 40.
- [47] L. Truffault, B. Choquet, K. Konstantinov, T. Devers, C. Couteau, L. J. Coiffard, *J. Nanosci. Nanotechnol.* **2011**, *11*, 2413.
- [48] H. Bemana, S. Rashid-Nadimi, *Electrochim. Acta* **2017**, *229*, 396.
- [49] C. Xia, Y. Jia, M. Tao, Q. Zhang, *Phys. Lett. A* **2013**, *377*, 1943.
- [50] S. G. Kakade, Y.-R. Ma, R. S. Devan, Y. D. Kolekar, C. V. Ramana, *J. Phys. Chem. C* **2016**, *120*, 5682.
- [51] G. Liu, Y. Zhao, N. Li, R. Yao, M. Wang, Y. Wu, F. Zhao, J. Li, *Electrochim. Acta* **2019**, *307*, 197.
- [52] Y. Huang, L.-W. Jiang, H. Liu, J.-J. Wang, *Chem. Eng. J.* **2022**, *441*, 136121.
- [53] W.-J. Jiang, T. Tang, Y. Zhang, J.-S. Hu, *Acc. Chem. Res.* **2020**, *53*, 1111.
- [54] S. Kment, P. Schmuki, Z. Hubicka, L. Machala, R. Kirchgeorg, N. Liu, L. Wang, K. Lee, J. Olejnicek, M. Cada, *ACS Nano* **2015**, *9*, 7113.
- [55] J. H. Kennedy, K. W. Frese, *J. Electrochem. Soc.* **1978**, *125*, 723.
- [56] M. Rioult, H. Magnan, D. Stanesco, A. Barbier, *J. Phys. Chem. C* **2014**, *118*, 3007.
- [57] T. S. Atabaev, H. H. T. Vu, M. Ajmal, H.-K. Kim, Y.-H. Hwang, *Appl. Phys. A* **2015**, *119*, 1373.
- [58] T. Käambre, M. Vanags, R. Pärna, V. Kisand, R. Ignatans, J. Kleperis, A. Šutka, *Ceram. Int.* **2018**, *44*, 13218.
- [59] Y. Zhang, S.-Y. Yuan, Y. Zou, T.-T. Li, H. Liu, J.-J. Wang, *Appl. Mater. Today* **2022**, *28*, 101552.
- [60] J. A. Glasscock, P. R. Barnes, I. C. Plumb, N. Savvides, *J. Phys. Chem. C* **2007**, *111*, 16477.
- [61] P. Tang, J. Arbiol, *Nanoscale Horizons* **2019**, *4*, 1256.
- [62] Y. Zhang, Y. Huang, S. S. Zhu, Y. Y. Liu, X. Zhang, J. J. Wang, A. Braun, *Small* **2021**, *17*, 2100320.